Oxidation of Metals, Vol. 45, Nos. 3/4, 1996

Microstructural Evidence for Short-Circuit Oxygen Diffusion Paths in the Oxidation of a Dilute Ni–Cr Alloy

C. K. Kim* and L. W. Hobbs*

Received October 27, 1994; revised April 24, 1995

A comparative study of high-temperature oxidation of Ni containing 1 at.% Cr and pure Ni was carried out. Instead of the conventional kinetics study using thermogravimetry, a microlithographic marker experiment was designed. Observation of the markers using cross-sectional TEM and SEM has revealed striking differences in the scale morphology, microstructures, and oxidation mechanisms between pure Ni and the Cr-doped Ni substrates. In particular, the results suggest that a small addition of Cr promotes significant inward transport of oxygen. Marker experiments revealed that NiO grown on pure Ni is wholly attributable to outward-cation diffusion. In contrast, NiO grown on Ni–1 at.% Cr exhibited formation of a substantial inner layer having a submicron grain size, established by the markers to have formed from oxygen ingress. For pure Ni, voids were observed to be distributed only within oxide grains. In contrast, for Ni containing 1 at.% Cr, elongated pores formed extensively along oxide-grain boundaries. Formation of new fine-grain oxide in these pores was observed to have sometimes completely resealed the void. It is, therefore, proposed that the transport of oxygen in the case of oxide scale grown on Ni–1 at.% Cr occurs via voids (pores) formed by vacancy coalescence at the grain boundaries.

KEY WORDS: short-circuit diffusion path; photolithographic marker; Ni and Ni–1 at.% Cr oxidation.

INTRODUCTION

There is considerable interest in the influence of small impurities in oxide growth at high temperature, since these additions can alter oxide micro-

*Massachusetts Institute of Technology, 77 Massachusetts Ave, Room 4-051, Cambridge, Massachusetts 02139.

0030-770X/96/0400-0247$09.50/0

structures and the kinetics of oxidation significantly. However, the effects of dilute impurities on the scale-growth mechanism do not appear to have been fully established, although simple oxidation paths have been suggested. Traditionally, oxygen diffusion in oxides has received much less attention than cation diffusion, therefore, the mechanism of oxygen transport on scale growth in the atomic, molecular, or ionic form has been poorly understood.

High-temperature oxidation generally produces duplex-oxide morphologies, designated as inner and outer layers. Many theories have been proposed to explain the origin of inner-layer oxides grown on pure metals and alloys. The classical models to explain the development of duplex-oxide growth were suggested by Mrowec[1] and Gibbs and Hales,[2] which were based on the dissociation of the oxide scale. Yurek and Schmalzried[3] observed porosity formation and migration across single-crystal cobalt oxide under an oxygen potential gradient. This mechanism also includes the dissociation of the oxide.

Microfissures within the oxide scales have been considered as a possible alternative explanation for duplex-scale growth which requires ingress of oxygen through oxide scales. Atkinson, Moon, Smart *et al.*[4–11] proposed a dynamic-fissure model which suggests that growth of new oxide within the scale can initiate the opening of pores. In their model existing pores are subsequently resealed, and new pores open continuously. The triple points of grain-boundary intersections and microvoids continuously created and rearranged by oxide creep were speculated as short-circuit diffusion paths by Robertson and Manning.[12] Evans *et al.*[13] argued that slip systems restricted by alloying elements can create porosity which subsequently leads to duplex growth. Grain-boundary sliding was suggested by Kofstad[14] for the possible mechanism of porosity formation during oxidation. However, unambiguous observations of pipelike channels have not been reported from these studies.

These theories were suggested without microstructural information, or even if microstructural studies were performed their descriptions have largely been limited to light microscopy or scanning electron microscopy (SEM) which limits the observation of important internal submicron microstructural details. Therefore, we cannot exclude the possibility that the real aspects of microstructural details of the oxide scales have been overlooked due to limitations of these investigating tools.

The purpose of this investigation was to achieve a micro- and nanometer characterization of the oxide morphologies for nickel oxidation by the application of transmission electron microscopy (TEM), in order to attain a thorough understanding of the processes occurring during the oxidation of a simple model system such as the oxidation of pure Ni and Ni–1 at.% Cr. In this study, appropriate TEM techniques for the observation across the

mature oxide scales were performed to investigate the effects of dopants in detail on the microstructure of oxide formation.

In order to investigate the effect of the dilute alloying addition, a microlithographic-marker experiment was performed instead of the conventional kinetics study such as thermogravimetry. In order to extract reliable information from a marker experiment, precautions should be exercised since markers may interfere with the oxidation process and development of microstructure in the oxide layers. Ideal markers should not react with the system during the oxidation process. They must remain immobile with respect to the system and have appropriate dimensions so that they will not interfere with the oxidation process. When all of these requirements are met, the markers should indicate the position of the original substrate surface prior to oxidation and reveal the location of new oxide formation within a scale, essentially demonstrating the proportions of inward and outward growth. The success of cross-sectional TEM (XTEM) and Auger electron spectroscopy (AES) in revealing the microstructural origins of morphological features in semiconductor devices[15] suggested that micromarkers of appropriate dimensions for electron microscopy could be laid down using standard microlithographic-deposition methods regularly employed in the manufacture of microcircuits. The facile control of size and spacing of markers provided by these methods ensures that markers spaced closely enough to be encountered frequently in TEM investigations but widely enough not to seriously interfere with oxidation kinetics or microstructural development can be generated.[16] This novel microlithographic-marker technique eliminates problems such as irregularity of deposition and adventitious location which are frequently encountered during other microscale-marker applications.[17–22]

EXPERIMENTAL PROCEDURES

Sample Preparation and Surface Pretreatment Prior to Oxidation

High-purity Ni (99.99%) and Cr (99.99%) were arc-melted in an argon atmosphere to form a Ni–1 at.% Cr alloy. After drop-casting, the alloy was cold-rolled to 0.5-mm thickness. Strips of the pure Ni and Ni–1 at.% Cr, $10 \times 25 \times 0.5$ mm, were cut from the sheet. The samples were mechanically polished sequentially from 600-grit SiC paper, 6-μm an 1-μm diamond paste down to 0.05-μm alumina powder. These samples were cleaned in solvents in the sequence of trichloroethylene, acetone, and methyl alcohol. After cleaning, samples were encapsulated in a vycor tube, evacuated to 1.5×10^{-4} Pa, and annealed in argon at 1123 K for several hours to achieve an average grain size of 200 μm.

Microscopic-Marker Deposition

Microscopic markers were deposited using photolithography, sputtering, and lift-off processes. Considerable effort was made to optimize the photolithographic process due to the reflectivity of the metal substrate compared to Si wafers and the greater difficulty in achieving flat, highly-polished surfaces.

The sequence of the photolithographic marker deposition is schematized in Fig. 1.

Mask Fabrication

The mask used for photolithographic-contact printing was prepared as a glass plate with a chromium coating on one side onto which the marker patterns were etched. For this study, the basic pattern consisted of an 8×8 array of 2.55×2.55 mm squares each containing 256 parallel lines 1 μm wide and spaced 10 μm apart. This pattern was produced by a $10\times$ reduction from an original array of parallel lines of this width, and the spacing was chosen to maximize the probability of finding the markers in XTEM with minimal disruption of the oxidation process.

Photolithography

After final mechanical polishing and cleaning, samples were coated with Shipley 820-20 photoresist and spun at 6000 rpm for 30 sec to achieve a film thickness of about 1 μm. Coated samples were then soft-baked in a convection oven at 353 K for 30 min to remove the major portion of the solvent. Contact printing through the mask was performed using a mask aligner (Karl Suss model 505) and an illuminating wavelength of 365 nm. Because the surface flatness varies from sample to sample, some overexposure was required to guarantee an undercut profile in the photoresist. Typically, an exposure time of 1.5 sec with light intensity of 600 J/m^2 produced good results. The exposed substrates were then developed in alkaline aqueous solution (Shipley 934 developer) for 60 sec, rinsed in hot water for an additional 60 sec, dried, and stored for marker deposition.

Deposition and Lift-Off

Marker patterning was achieved by applying a lift-off technique. Composite markers comprising an initial 10-nm-thick layer of Mo under a 150-nm-thick layer of Pt marker material were Ar-plasma sputtered onto the substrates using a sputtering system (MRC model 8620). The samples were then immersed in Shipley stripper A-20 or acetone to remove the remaining photoresist, leaving the marker pattern shown in Fig. 2. As SEM micrograph

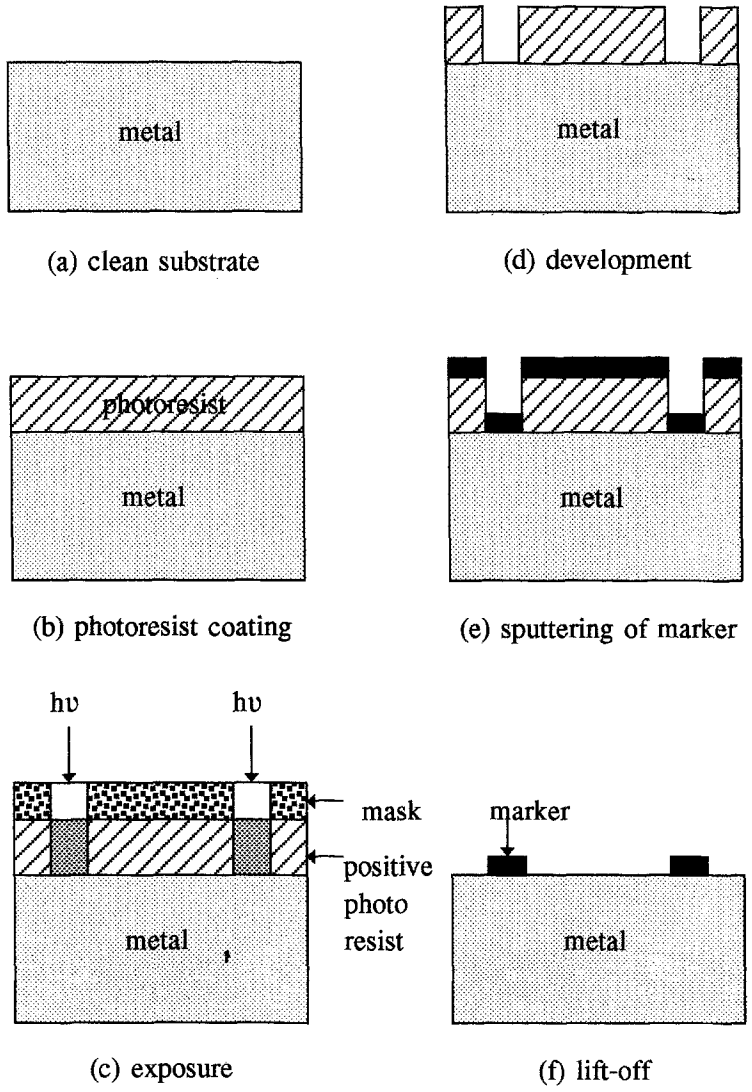

Fig. 1. Schematic representation of processing sequences for the photolithographic-marker deposition.

in Fig. 2 illustrates the high resolution achievable through this microphotolithographic process. The initial Mo (BCC) layer in the composite marker was found necessary to act as a diffusion barrier precluding dissolution of the Pt marker (Fcc) into the Ni-base substrate (Fcc) during oxidation. It

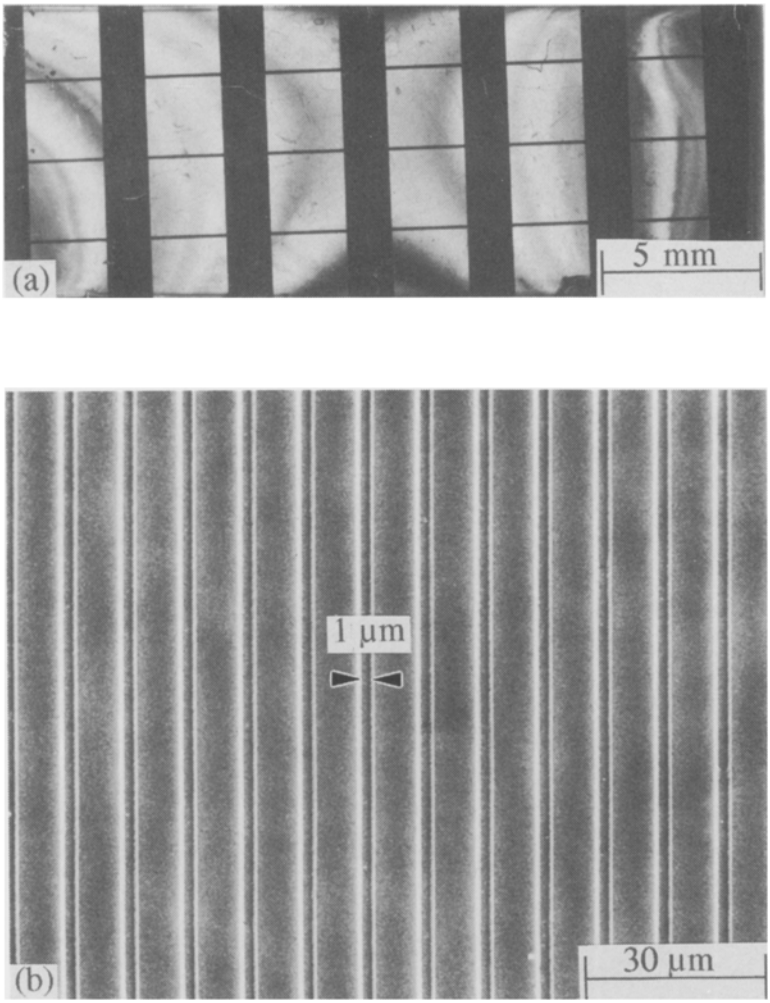

Fig. 2. (a) Optical light micrograph of the marker pattern generated on Ni–1 at.% Cr substrate before oxidation. (b) SEM micrograph of the markers generated in one of the squares shown in (a).

was reported that Mo did not affect the high-temperature oxidation behavior of some dilute nickel- and cobalt-base alloys.[23]

Oxidation Experiments

Samples with and without markers were oxidized at 1273 K in air for various times and subsequently examined by SEM, TEM, and scanning-

transmission-electron microscope (STEM) observation. The temperature of the oxidizing furnace was maintained within 5 K of the set point.

Observation of Oxide Microstructures

Parallel and transverse (cross) section specimens with respect to the scale–substrate interface were prepared for both SEM and TEM/STEM observations. The techniques for preparation of parallel and transverse TEM samples are well reviewed.[15,24] To avoid complications arising from convolution of the oxide near the edges of the specimens, the strips for preparation of the parallel and transverse sections were chosen from the centers of specimens.

A SEM (Amray model 1000A and Cambridge model 250MK3) was used for the observation of the surface of the oxide and for the location of the marker positions in the oxide scale for longer-time oxidation. The SEMs were operated mainly at 20 kV.

TEM (JEOL model 200CX) observation was accomplished at 200 kV. STEM (VG model HB501) observation was made at 100 kV using a field-emission gun equipped with an energy-dispersive X-ray windowless detector (VG model LINK LZ-5).

RESULTS

Microlithographic-Marker Experiment

Oxidation in air at 1273 K produced very different results for pure Ni and for Ni–1 at.% Cr alloys (Fig. 3). In both cases, however, the markers are seen to remain substantially intact and embedded in a scale thickness of 10–20 μm. The regularity of the marker pattern eliminates any ambiguity in marker identification, a problem with other micromarker techniques. For pure Ni (Fig. 3a), the markers were found very close to the substrate–scale interface. A little oxide has formed immediately beneath each marker, indicating a minor local perturbation of the oxidation process by the markers, but the fact that the unperturbed portion of the scale–substrate interface lies along the line of the markers confirms that the interface has not moved appreciably during scale growth. We, therefore, conclude that oxidation is taking place essentially solely at the oxide–gas interface, necessarily by migration of Ni cations through the scale.

By contrast, for Ni–1 at.% Cr (Fig. 3b), the markers are embedded well into the scale at the interface between two oxide layers, the lower of which appears to be highly porous. XTEM (Fig. 4) indeed reveals the markers at the juncture of these two layers, the upper of which is columnar oxide similar to that formed on pure Ni, the lower of which is extremely fine grain but

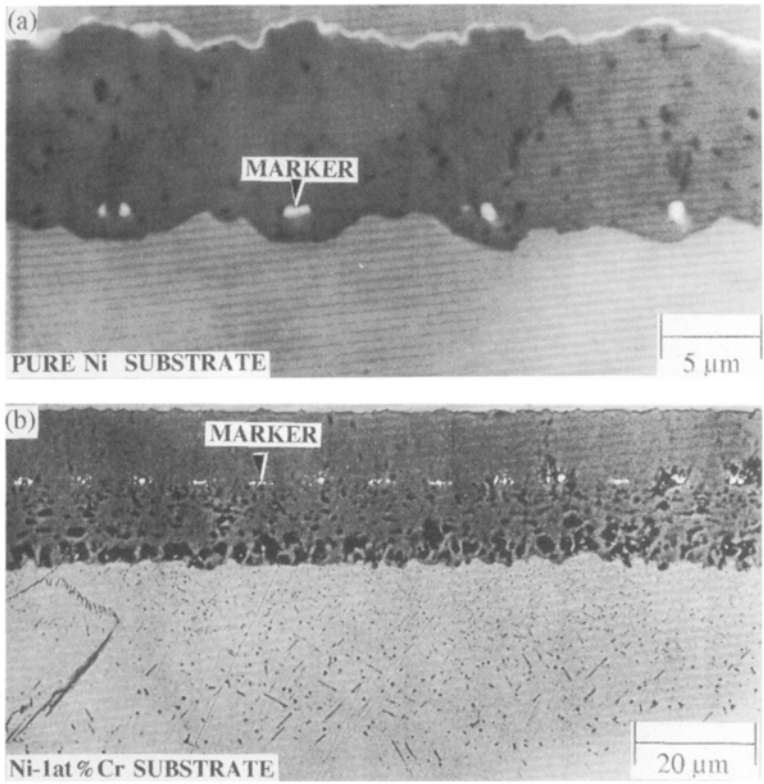

Fig. 3. (a) Transverse-sectional SEM micrograph (backscattered image) of oxide formed on pure Ni oxidized in air for 1 hr at 1273 K, showing markers embedded close to the oxide–metal interface. (b) Transverse-sectional SEM micrograph of oxide scale formed on Ni–1 at.% Cr oxidized in air for 5 hr at 1273 K, showing markers located at the inner–outer scale interface.

nevertheless compact. It has long been argued by many researchers whether the dark holes in the inner layer observed using light microscopy or SEM represented porosity.[1–3] The mechanism for porosity formation was based on the dissociation of the oxide scale. Such pores and voids have not been observed in the XTEM work in this research. The porous appearance of this layer in SEM, often remarked upon in observations by light microscopy of duplex scales, is in fact an artifactual result of grain pullout during metallographic polishing. The formation of this layer does not therefore seem likely to occur by a dissociative mechanism. Consequently, several models based on the available sites such as voids or pores which are created by the

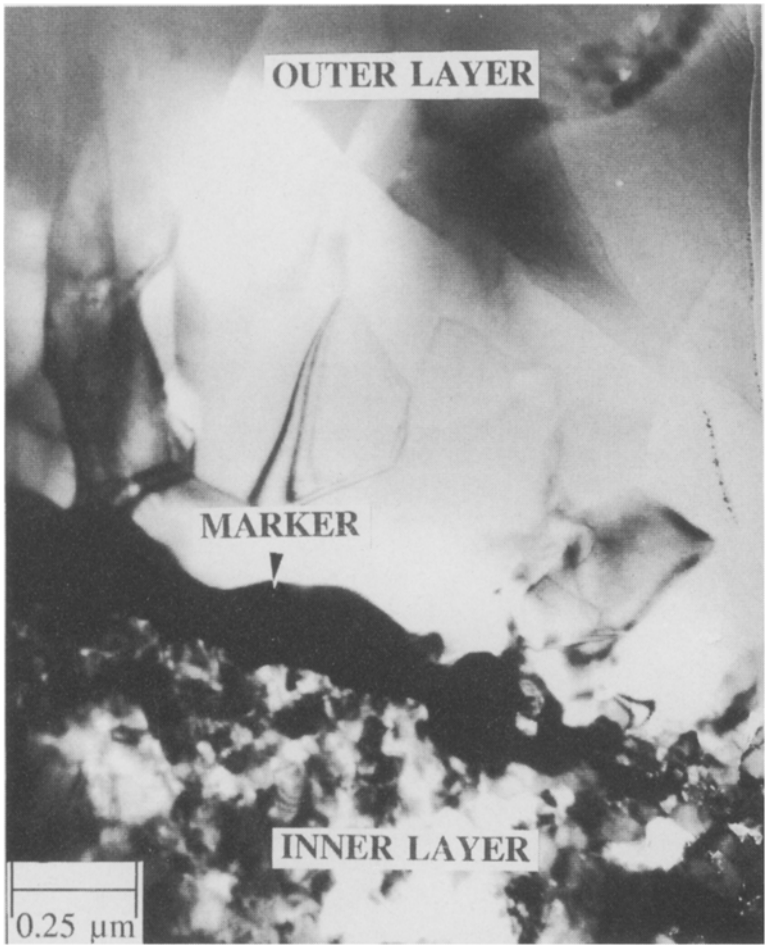

Fig. 4. XTEM image of NiO scale formed on Ni–1 at.% Cr substrate oxidized for 15 min at 1273 K in air, showing a marker embedded in the scale at the interface between fine-grain inner layer and large, columnar outer-layer scales.

dissociative mechanism for the inner-layer growth are questionable. A SEM micrograph of Ni–1 at.% Cr also exhibits an internal oxidation zone below the oxide scale; which is α-Cr_2O_3 (STEM and electron diffraction) (Fig. 5). The composition of the fine-grain inner layer is, however, single-phase NiO, which the marker position reveals to have formed by inward transport of oxygen.

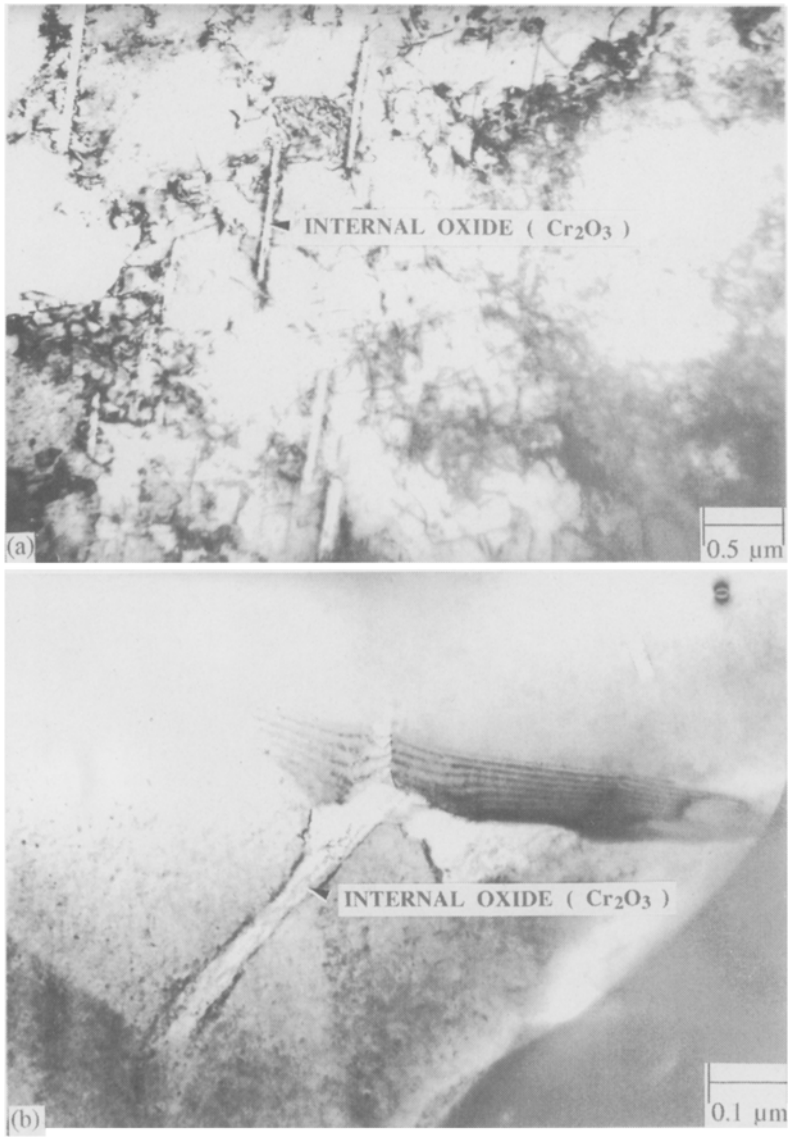

Fig. 5. TEM transverse-section image of the Ni–1 at.% Cr substrate after oxidation for 15 min at 1273 K showing (a) internal oxide particles and (b) internal oxide formation at the grain boundary of the metal substrate.

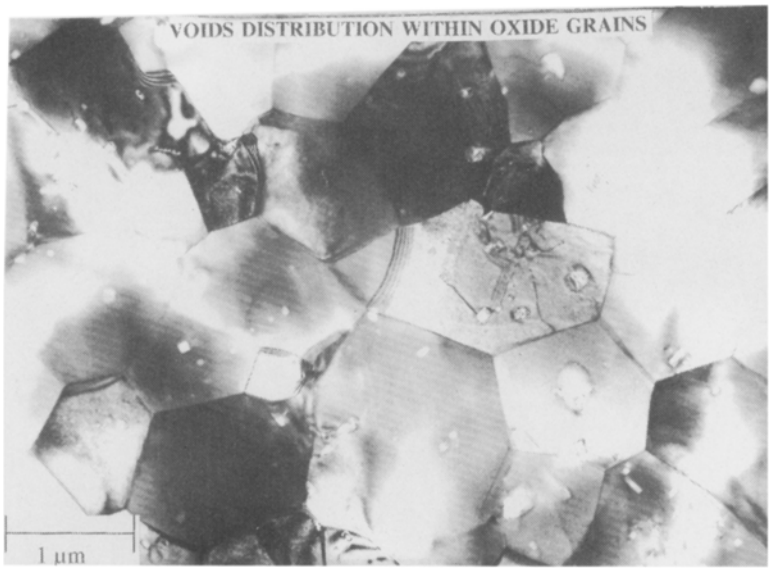

Fig. 6. TEM parallel-section image near the oxide–gas interface of the oxide grown on pure Ni at 1273 K for 2 hr, showing formation of most voids inside the grains.

Microstructure of Oxides Grown on Pure Ni and Ni–1 at.% Cr

For pure Ni, voids were observed to be distributed only within oxide grains (Fig. 6). In contrast, for Ni containing 1 at.% Cr, elongated pores formed extensively along oxide-grain boundaries (Figs. 7 and 8). Formation of new fine-grain oxide (Fig. 9) in these pores was observed to have sometimes completely resealed the voids (Fig. 10).

The Observed Movement of Vacancies during Oxidation

During the initial stage of oxidation, Ni vacancies created at the oxide–gas interface diffuse throughout the oxide scale existing in the form of a solid solution in the oxide. As a result, nonstoichiometry in $Ni_{1-x}O$ due to aliovalent cation doping is accommodated by long-range ordering of point defects (vacancies and aliovalent cations), representing a tendency toward spinel-like ordering, which generates a defect superstructure (Fig. 11). As the oxidation time increases, the vacancies precipitate as voids at the grain boundaries or form vacancy-dislocation loops. Voids formed along grain boundaries in Ni–1 at.% Cr (Fig. 7), while voids were observed entirely inside the grains in pure Ni (Fig. 6). Pores formed along grain boundaries due to the coalescence of the voids. These large pores due to the coalescence

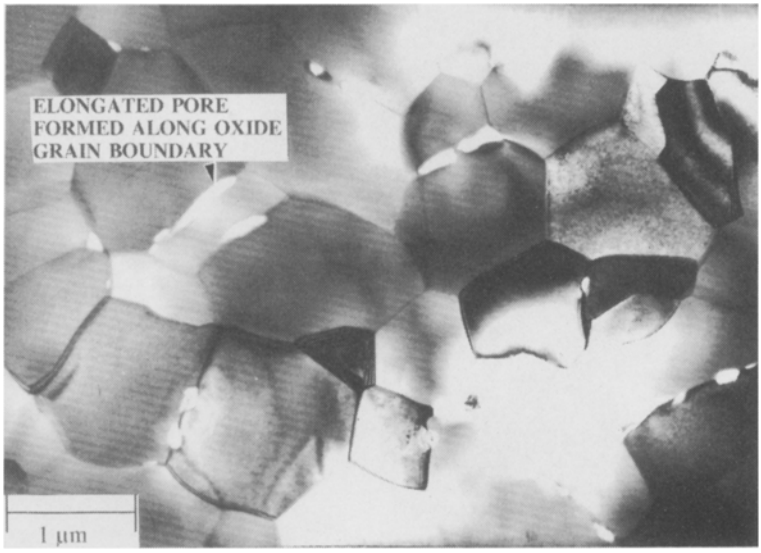

Fig. 7. TEM parallel-section image near the oxide–gas interface of oxide grown on Ni–1 at.% Cr at 1273 K for 2 hr, showing elongated pores along the columnar-oxide grain boundaries.

of voids along the grain boundaries might be misinterpreted as the dissociation of the oxide which was reported to occur by other researchers at oxide-grain boundaries. These pores may act as short-circuit-diffusion paths for oxygen molecules. In this experiment, the injection of the vacancies did not appear to occur since any apparent voids or dislocation loops were not found in the metal substrate.

DISCUSSION

Oxygen Pathway for Inner-Layer Growth

New oxide growth at the metal–oxide interface, observed in the marker experiment, requires the oxidant to be transported across the oxide layer. If the transport of both Ni and O during film growth is by solid-state diffusion along grain boundaries, then the grain-boundary-diffusion coefficient for O would have to be 1% of that for Ni at 1000°C. The estimated grain-boundary-diffusion coefficient for O at 1000°C is about 5×10^{-12} cm^2 s^{-1}.[25-27] Therefore, solid-state, grain-boundary diffusion will be much too slow (probably by about two to three orders of magnitude) to account for the observed microstructural growth (~1:1 ratio of inner and outer layers, Fig. 3b).

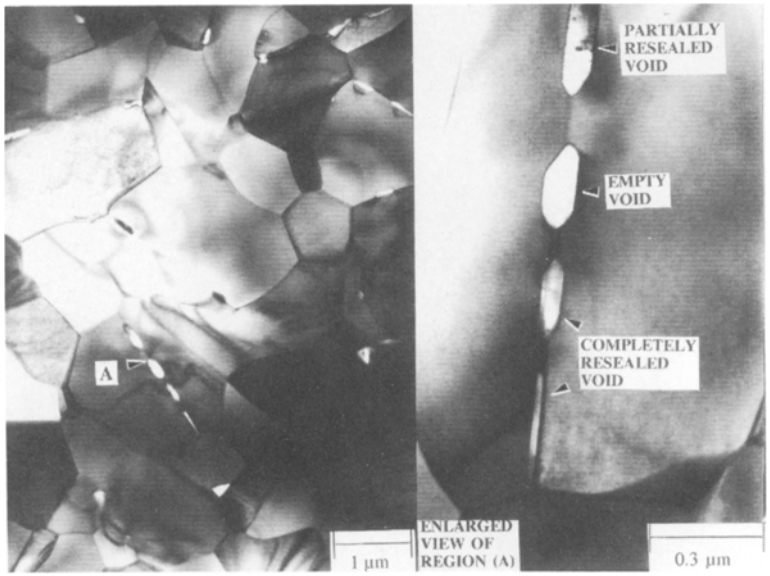

Fig. 8. TEM parallel-section image midway through the oxide scale grown on Ni–1 at.% Cr at 1273 K for 2 hr, showing voids formation along the oxide grain boundaries: Inset represents an enlarged view of region A.

Therefore we suggest that inner-layer growth should be dominated by gaseous-oxygen transport and some type of short-circuit path is required for the oxidant to be transported through the scale.

It is proposed, in this study, that oxygen pathways for the formation of the inner layers for oxide grown on Ni–1 at.% Cr for long-time oxidation are associated with the pores created due to void coalescence along the grain boundaries. For short-time oxidation, oxygen transport appears to be achieved along the grain boundaries in an ionic form with a slower mobility than molecular oxygen transport, so that the portion of the columnar layer is larger than that of the inner layer. For long-time oxidation, oxygen is transported efficiently along grain boundaries through the void structure, which results in an abundant amount of oxygen ingress for the mature growth of the inner layer, in turn leading to the 1:1 ratio of the inner and outer layers (Fig. 3b). These oxygen pathways formed along grain boundaries can be resealed; therefore these processes appear to be dynamic due to the newly formed oxides at the voids (Figs. 8–10). We believe that this dynamic nature of voids, i.e., continuous creation and resealing of the voids, makes it difficult to observe unambiguous pipelike pores in XTEM oxide micrographs.

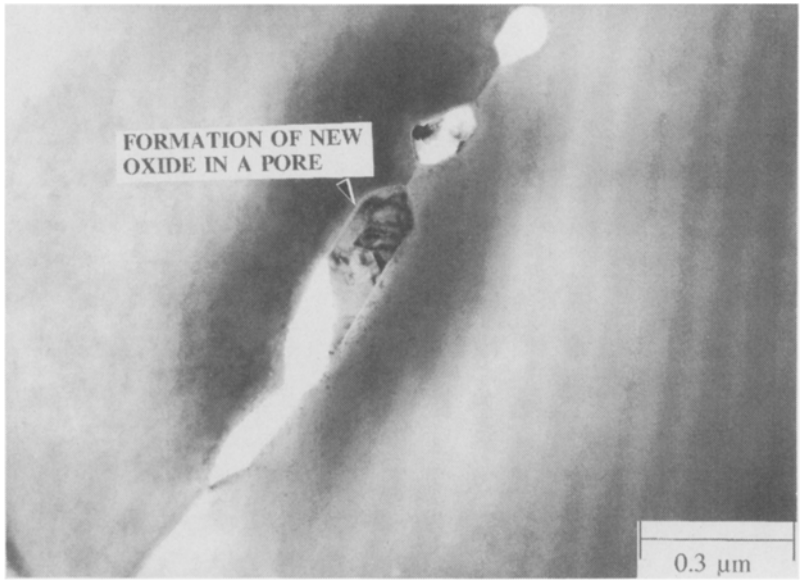

Fig. 9. TEM parallel-section image of the oxide near the scale–gas interface grown on Ni–1 at.% Cr at 1273 K for 2 hr in air, showing formation of new fine-grain oxide in the pore.

Observed Oxide Growth on Ni–1 at.% Cr

As soon as oxidation begins, oxygen ingress occurs immediately to form Cr_2O_3 internal oxide in the Ni–1 at.% Cr substrate (Fig. 5). An initial inner-layer NiO scale forms and over it the beginnings of a columnar outer layer. Short-circuit paths in the outer layer begin to open up, and new fine-grain oxide begins to form at the metal–inner-scale interface, supplanting or displacing the initial inner layer. As this new inner-layer oxide advances into the metal substrate, the Cr_2O_3 internal oxides are engulfed by the inner-layer oxide which formed by oxygen ingress, and Cr_2O_3 undergoes dissolution into the NiO. As a result, the distribution of Cr is confined to the inner-layer grain boundaries; in this study, grain-boundary segregation of Cr was not detected at the outer-columnar grain boundaries up to 1 hr oxidation, while Cr segregated at the inner-layer grain boundaries (Fig. 12), which indicates that the cation transport along outer grain boundaries is still the dominant transport mechanism. It should be noted also that voids are not observed in this scale, suggesting that void formation is associated with Cr segregation at the columnar grain boundaries. Therefore, formation of a duplex scale due to the blocking of cation transport by outer, grain-boundary segregation,

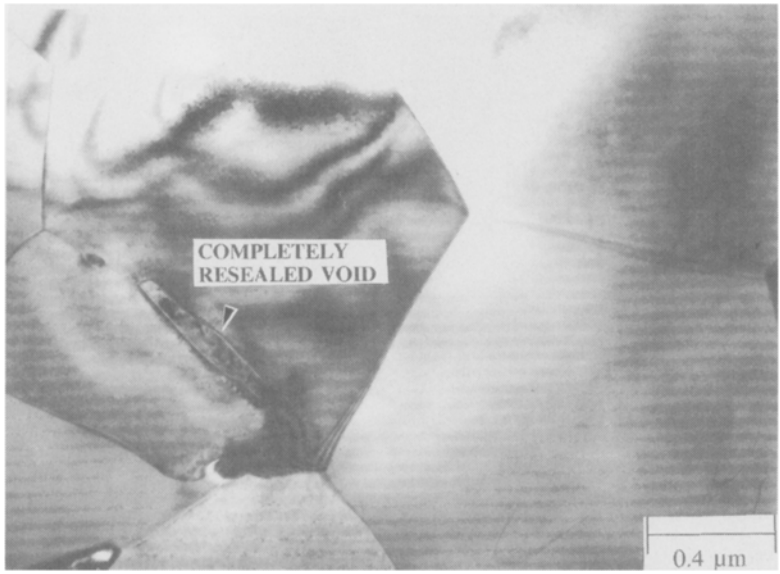

Fig. 10. TEM parallel-section micrograph of the oxide midway through the scale grown on Ni–1 at.% Cr at 1273 K for 2 hr in air, showing completely resealed voids due to formation of new oxide in the void.

i.e., anion transport along grain boundaries and cation transport through the lattice, is not likely to have occurred.

Cr segregation along inner-layer oxide grain boundaries appears to hinder short-circuit diffusion of Ni during scale growth. However, Cr segregation does not have any effect on O transportation along grain boundaries since Cr occupies the cation-transport sites of the oxide. The grain boundaries of the outer columnar layer subsequently developing continue to serve as short-circuit-diffusion paths for cation transport, since no segregant (Cr) has blocked this short-circuit-difffusion path. Consequently, the inner and outer layers grow simultaneously in opposite directions. The ratio of the inner layer to outer layer of oxide increases with time, but the ratio of the inner to outer layer never reaches 1:1 until oxygen transport appears to occur via well-defined pores formed along grain boundaries. It is observed that it takes 2 hr of oxidation at 1000°C to reach a 1:1 ratio. After 2-hr oxidation, Cr was detected by STEM at the outer-columnar grain boundaries (Fig. 13). It is, therefore, speculated that Cr segregation at the outer-columnar grain boundaries is associated with void formation at grain boundaries for Ni–1 at.% Cr oxidation. The inner-layer thickness never exceeds this maximum fraction (in our study about 0.5) of the total thickness even after 5 hr of oxidation.

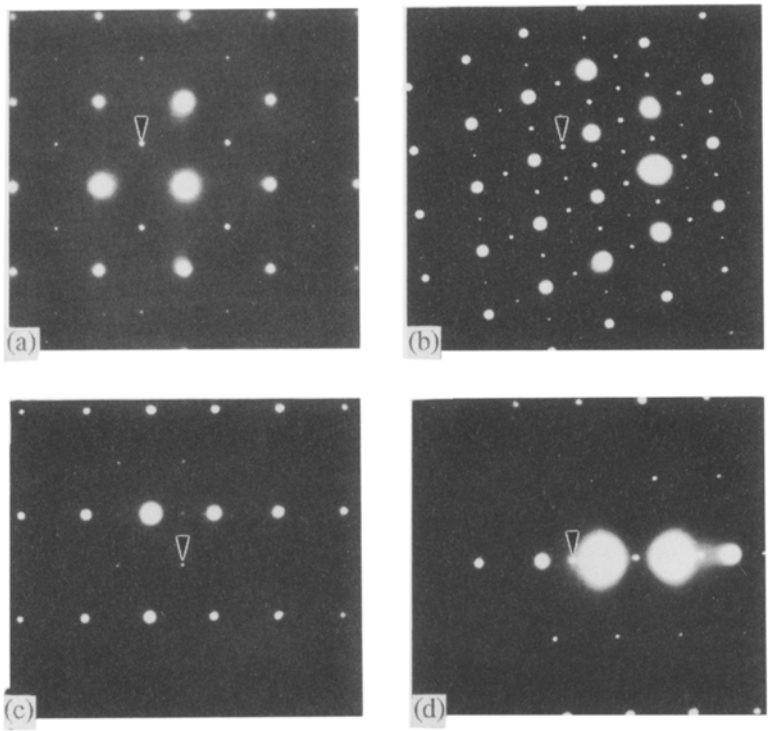

Fig. 11. Electron-diffraction patterns of several low-index poles taken from NiO columnar grains formed on Ni–1 at.% Cr by oxidation at 1273 K for 1 hr, exhibiting structurally forbidden reflections (the weaker reflections, pointed by arrows, are forbidden to the *Fm*3*m* structure of NiO): (a) (100) reciprocal-lattice plane, (b) (110) reciprocal-lattice plane, (c) (112) reciprocal-lattice plane, (d) (123) reciprocal-lattice plane.

The interface between the inner layer and the outer columnar layer marks the position of the original metal surface. During oxidation, grain growth of the columnar oxide grains seems only to occur in an outward direction toward the oxide–gas interface. This appears to be due to specific concave curvature of grains which is observed on the surface of oxide. Eventually this outward, columnar-grain growth will lead to a texture formation of outer columnar layer.

In this research, even without a detailed kinetics study, the slightly faster growth rate of oxide growth on Ni–1 at.% Cr was apparent in TEM investigations for up to 1 hr oxidation. This is largely ascribable to the formation of the inner-layer scale. With the formation of an inner layer, the new oxide grows at the metal–oxide interface as well as at the outer oxide–

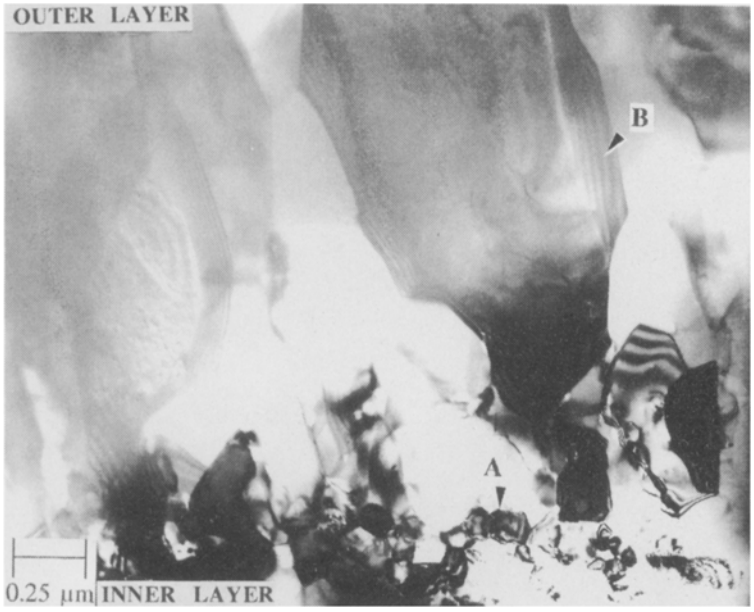

Fig. 12. TEM transverse-section image of the oxide grown on Ni–1 at.% Cr at 1273 K for 1 hr, showing the interface region between the large columnar layer and the inner layer and the existence of a layer with the intermediate size grains which is presumably caused by the growth of the small, inner-layer oxide grains: (A) Cr segregation at grain boundaries of fine-grain oxide was detected by STEM; (B) Cr segregation at grain boundaries of columnar oxide was not detected.

gas interface. Another possible cause for the faster growth is that inner layers are composed of very small grains which contribute to a large area of short-circuit paths. However, the segregation of Cr in the inner-layer grain boundaries appears to offset the increase in the oxidation rate that results from the doping and grain-size effects on NiO of the Cr alloying addition. Thus, the effect of Cr doping on the oxidation rate is seen to be not just a matter of doping-induced vacancy generation but a more complex interaction of microstructural consequences of doping.

Voids Reported in the Literature

There have been other reports of voids in scale.[14,28,29] Choquet *et al.* observed microporosity.[28] However, this porosity was associated with relatively large grains only in a few areas. Porosity reported by Yang *et al.* is predominantly intergranular, which is different from that observed in oxide grown on Ni–1 at.% Cr.[29] Kofstad observed porosity and considered it as a possible candidate for a microchannel.[14] Oxide-growth stress may be relieved

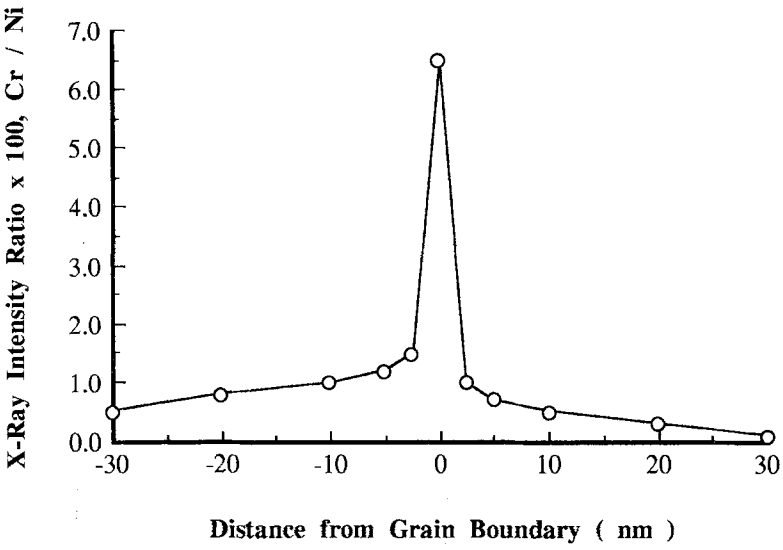

Fig. 13. Concentration profile determined by STEM in the outer, columnar-layer oxide grain boundary grown on Ni–1 at.% Cr at 1273 K for 2 hr.

by both diffusional creep and grain-boundary sliding in the oxide or alloy substrate. However, stress relief is more difficult for scales with columnar microstructures than for fine, equiaxed grains because grain-boundary sliding is not likely to occur for a columnar microstructure.[30,31] Consequently, this mechanism does not operate during oxidation of Ni–1 at.% Cr alloy since observed oxide scale consists of columnar microstructures. Voids in α-Al_2O_3 were reported by Pint *et al.*[32,33] Very few voids were observed in the doped alumina scale. Large voids were present in the undoped scale. These voids were observed to be contained entirely within each grain and were not connected to each other or to adjacent boundaries. Therefore, these voids may provide discontinuous short-circuit pathways. Also, these voids are differently distributed comparing with those observed in the oxide grown on Ni–1 at.% Cr.

CONCLUSIONS

Microscopic markers can be regularly and reliably deposited by the photolithographic technique. Markers interfere only marginally with oxidation processes. Even after slight interaction is taken into account, markers are easy to locate and accurately represent interface positions. Marker experiments confirm that the oxide scale for pure Ni is the result of outward-cation diffusion, while a dilute alloying addition (1% Cr) causes substantial

oxygen ingress leading to significant inner-layer growth. Oxygen ingress in Ni–1 at.% Cr appears to occur via pores formed along grain boundaries.

ACKNOWLEDGMENTS

The financial support from the National Science Foundation is gratefully acknowledged.

REFERENCES

1. S. Mrowec, *Corros. Sci.* **7**, 563 (1967).
2. G. B. Gibbs and R. Hales, *Corros. Sci.* **17**, 487 (1977).
3. G. J. Yurek and H. Schmalzried, *Ber. Bunsen-Ges. Phys. Chem.* **79**, 255 (1975).
4. D. P. Moon, A. W. Harris, P. R. Chalker, and S. Mountfort, *Mater. Sci. Technol.* **4**, 1101 (1988).
5. D. P. Moon, *Oxid. Met.* **31**, 71 (1989).
6. A. Atkinson and D. W. Smart, *J. Electrochem. Soc.* **135**, 2886 (1988).
7. A. Atkinson, UKAEA Harwell Report **AERE-R12404** (1987).
8. A. W. Harris and A. Atkinson, UKAEA Harwell Report **AERE-R13421** (1989).
9. A. Atkinson, *Mater. Sci. Technol.* **4**, 1046 (1988).
10. A. Atkinson and D. W. Smart, UKAEA Harwell Report **AERE-R12762** (1987).
11. H. V. Atkinson, *Mater. Sci. Technol.* **4**, 1052 (1988).
12. J. Robertson and M. I. Manning, *Mater. Sci. Technol.* **4**, 1064 (1988).
13. A. G. Evans, D. Rajdev, and D. L. Douglass, *Oxid. Met.* **4**, 151 (1972).
14. P. Kofstad, *Oxid. Met.* **24**, 265 (1985).
15. R. B. Marcus and T. T. Sheng, *Transmission Electron Microscopy of Silicon VLSI Circuits and Structures* (Wiley, New York, 1983), p. 19.
16. C. K. Kim, S. K. Fan, and L. W. Hobbs, in *Microscopy of Oxidation*, G. J. Lorimer, ed. (Institute of Metals, 1991), p. 374.
17. B. L. Gleeson, D. L. Douglass, and F. Gesmundo, *Oxid. Met.* **31**, 209 (1989).
18. E. M. Fryt, G. C. Wood, F. H. Stott, and D. P. Whittle, *Oxid. Met.* **23**, 77 (1985).
19. H. M. Hindam and W. W. Smeltzer, *Oxid. Met.* **14**, 337 (1980).
20. C. M. Cotell, K. Przybylski, and G. J. Yurek, in *Fundamental Aspects of High Temperature Corrosion*, Vol. 2, D. A. Shores and G. J. Yurek, eds. (The Electrochemical Society, Pennington, NJ, 1986), p. 103.
21. E. W. A. Young, H. E. Bishop, and J. H. de Wit, *Surf. Interface Anal.* **9**, 163 (1986).
22. T. A. Ramanarayanan, R. Ayer, R. Petkovic-Luton, and D. P. Leta, *Oxid. Met.* **29**, 445 (1988).
23. F. H. Stott, I. G. Wright, T. Hodgkiess, and G. C. Wood, *Oxid. Met.* **11**, 141 (1977).
24. L. W. Hobbs and T. E. Mitchell, in *High Temperature Corrosion*, R. A. Rapp, ed. (NACE-6, Houston, 1983), p. 76.
25. P. Kofstad, *JIMIS-3* Suppl., 1 (1983).
26. A. Atkinson and R. I. Taylor, UKAEA Harwell Report **AERE-R11763** (1985).
27. A. Atkinson, D. W. Smart, and R. I. Taylor, UKAEA Harwell Report **AERE-R12751** (1987).
28. P. Choquet and R. Mevrel, *Mater. Sci. Eng.* **A120**, 153 (1989).
29. C. H. Yang, G. E. Welsch, and T. E. Mitchell, *Mater. Sci. Eng.* **69**, 351 (1985).
30. J. Stringer, *Corros. Sci.* **10**, 513 (1970).
31. A. G. Evans and R. M. Cannon, *Mater. Sci. Forum* **43**, 243 (1989).
32. B. A. Pint, J. R. Martin, and L. W. Hobbs, *Oxid. Met.* **39**, 167 (1993).
33. B. A. Pint and L. W. Hobbs, *Oxid. Met.* **41**, 203 (1994).